VIRTUAL AND PHYSICAL PROTOTYPING
2022, VOL. 18, NO. 1, e2131583 (19 pages)
https://doi.org/10.1080/17452759.2022.2131583

Taylor & Francis
Taylor & Francis Group

Novel method of residual stress reduction for AlSi10Mg manufactured using selective laser melting without compromise of mechanical strength

Chong Heng Lim [a,b], Hua Li [a], Manickavasagam Krishnan [b], Kewei Chen [a] and Junru Li [c]

[a]Singapore Centre for 3D Printing, School of Mechanical and Aerospace Engineering, Nanyang Technological University, Singapore, Singapore ; [b]Additive Manufacturing Group, Advanced Remanufacturing and Technology Centre, Agency for Science, Technology and Research (A*STAR), Singapore, Singapore; [c]College of Mechanical and Electrical Engineering, Qingdao University, Qingdao, People's Republic of China

ABSTRACT

AlSi10Mg is often used to fabricate functional parts by Laser Beam Powder Bed (LBPB) fusion but is limited by the residual stresses formed during the process. Conventional methods of stress relief of AlSi10Mg often compromise the mechanical properties due to the high-temperature used. This paper solves the dilemma by using a novel method of residual stress relief without compromising its mechanical properties. This process uses a lower temperature for treatment followed by uneven cooling, inducing thermal stress during the cooling process such that it cancels out the existing residual stress that remains. The compressive strength of the part was not compromised after this treatment, verified by microstructure images. From electron backscatter diffraction (EBSD) analysis, the change in density of low angle grain boundaries (LAGB) and magnitude of residual stress relieved via this method followed the same trend, indicating the induction of dislocations from the stress-induced during uneven cooling.

ARTICLE HISTORY
Received 9 September 2022
Accepted 27 September 2022

KEYWORDS
Selective laser melting; residual stress; AlSi10Mg; heat treatment; compressive behaviour

1. Introduction

Laser beam powder bed (LBPB) additive manufacturing, also commonly known as selective laser melting (SLM), is one of the techniques under powder-based systems that are capable of producing end-usable metal parts with complex geometries. AlSi10Mg is an excellent material suitable for fabrication via the LBPB process, as it has better mechanical properties as compared to that made by the conventional cast method (Yan, Song, and Shi 2020; Manfredi et al. 2014). The first successful application of AlSi10Mg in LBPB was done in 2010 (Karolus et al. 2019), spinning off further research of this methodology for the fabrication of this material.

Residual stress exists in materials that underwent processes involving heat followed by rapid cooling in the SLM process. The existence of residual stress in manufactured parts can result in premature failure even when subjected to loads within its design limits. Excessive residual stress is one of the limiting factors for the limited adoption of existing metal alloys in the LBPB process (Frazier 2014). Restrictions of development and application of the LBPB processed parts were described to be due to 'residual stress, defects, and columnar grains with anisotropy' (Zhang et al. 2016). Studies have been done to investigate the 'printability' of existing alloys based on common LBPB parameters (Mukherjee et al. 2016), and the residual stress that develops in each alloy is an important factor. Even if the residual stress does not result in significant dimensional warpage, residual stress that exceeds the yield limit of the material can result in plastic deformation (Kudryavtsev 1964), resulting in a poorer mechanical property causing premature failure below its operating load (Panontin and Hill 1996). Many different methods have been developed to address the problems associated with residual stress in the additive manufacturing process.

Residual stresses exist in equilibrium balanced by a combination of tensile and compressive stress within the body of parts, illustrated by the Heyn spring model (David 1999). While residual stress in a structure exists as a combination of tensional and compressional stresses at different regions (Karlsson 2005), tensional stress at the surface or subsurface would pose a higher risk of fatigue failure as compared to if it was compressional stress. Tensional residual stress on the surface is one of the main causes of initiation and propagation of cracks in weldment (Iida, Yamamoto, and Takanashi 1997)

CONTACT Chong Heng Lim LIMC0199@e.ntu.edu.sg; Hua Li LiHua@ntu.edu.sg Singapore Centre for 3D Printing, School of Mechanical and Aerospace Engineering, Nanyang Technological University, 50 Nanyang Avenue, Singapore 639798, Singapore

and thus, many studies on residual stresses are targeted in the surface or sub-surface region. The fatigue life of materials can be enhanced by inducing compressive residual stress on critical regions on the surface and sub-surface (Benachour, Benachour, and Benguediab 2016; Siddique 2005; McClung 2007; Reid 2003). Inducing compressive stress on the surface of glass and ceramics help to increase the strength of the material (Withers and Bhadeshia 2001).

The mechanism of residual stress induction during the LBPB process involves compressive stress induced on the top surface during heating and tensile stress during cooling (Mercelis and Kruth 2006). Restriction in expansion and contraction is the cause of residual stress to be induced between regions (Liu, Yang, and Wang 2016; Kruth et al. 2005; Morgan, Sutcliffe, and O'Neill 2004). A mathematical model by Mercelis successfully predicted the residual stress profile verified by experimental measurement, with residual stress induction due to shrinkage of the top upper layer (Mercelis and Kruth 2006).

Conventional post-heat treatment for AlSi10Mg manufactured by SLM involves annealing at 300 °C for 2 h to achieve residual stress relief. Unanimous result finding shows that the process results in poorer mechanical properties in terms of tensile strength, yield strength, and hardness, particularly after 2 h of treatment at 300 °C (Takata et al. 2017; Zhuo et al. 2019; Yang et al. 2018; Maamoun et al. 2018), 450°C, 500°C and 550°C (Li et al. 2016). After heat treatment at 300 °C for 2 h, the yield stress reduced by 20% to 35%, tensile strength reduced by 40%, and total elongation increased by 8.7% to 11.1% (Takata et al. 2017). Compressive strength was found to reduce the most (56% drop in compressive strength and 47% drop in compressive yield strength) as compared to tensile strength (11% to 12% reduction) after heat treatment (Aboulkhair et al. 2016). Other than observing the duration of treatment and temperature, the cooling must be slow and controlled (Shanmughasundaram and Dahle 2018), usually performed in the furnace itself with the cooling duration equivalent to or longer than the heat treatment itself. Many studies have been done on this heat treatment methodology (Zhuo et al. 2019; Yang et al. 2018; Padovano et al. 2020). This methodology has been optimised for stress relief and heat treatment at a lower temperature and a duration of 200 °C for 1 h is insufficient to relieve the stress completely (Maamoun et al. 2018). Another study found that treatment at a lower temperature of 250 °C is less detrimental to the tensile strength than at 300 °C (Mertens et al. 2015) but is not sufficient to achieve full residual stress relief (Mertens et al. 2015). The reduction in mechanical strength is attributed to the destruction of the Si network structure during heat treatment at a higher temperature. SEM (scanning electron microscope) images show obvious destruction of the Si network structures after treatment at 300 °C (Yang et al. 2018), but the network structure is still intact after treatment at a lower temperature of 160°C (Yang et al. 2018) and 200 °C (Rafieazad, Mohammadi, and Nasiri 2019).

Another popular conventional heat treatment for AlSi10Mg is the T6 heat treatment, with different modified versions being studied (Li et al. 2016; Yang et al. 2018) as it has been shown to improve mechanical properties of cast AlSi10Mg due to precipitation strengthening. Compressive strength was found to reduce the most (56%) in LBPB manufactured AlSi10Mg parts subjected to T6 heat treatment, as compared to other mechanical properties such as hardness (16–20%) and tensile strength (11–12%) (Aboulkhair et al. 2016).

After solution or aging heat treatment, the cooling process can be slow or via rapid quenching into a medium. In a study by Dong, parts subjected to a higher cooling rate have the largest compressive stress induced on their surface as compared to those exposed to a slower cooling rate (Dong et al. 2015). Upon being subjected to rapid cooling, tensile stress was found in the center portion deduced from the slitting method, and the residual stresses in the outer portion are compressive. This residual stress profile is similar to that induced in thermal tempering of glass. Due to the transparent nature of glass, the entire residual stress profile across the depth of glass can be measured non-destructively and accurately using scattered light polariscope. The mechanism of residual stress induction in thermal tempering of glass has been well established and modelled results are aligned with experimental results (Aydıner and Ustundag 2005). The distribution of the temperature and residual stress profile of tempered glass across its depth follows a parabolic curve (Varshneya and Mauro 2019). The compressive stress magnitude is approximately twice that of the tensile stress in the center, while the compressive layer depth forms 21% on the top surface and tensile stress forms 58% of the entire depth. Rapid cooling also induced a similar parabolic residual stress profile on Al-Cu alloy (Dong et al. 2015).

Studies have shown that heat treatment will reduce low-angle grain boundaries (LAGB) (Takata et al. 2017) due to the reduction of dislocations (Humphreys and Hatherly 2012). Results from past work also show the possible effect of induced residual stress resulting in strains that cause dislocation and an increase in LAGB. The experiment by Takada (Takata et al. 2017) shows a higher peak in LAGB after a 6 h duration of 530 °C

treatment followed by rapid cooling, as compared to that of a 2 h duration treatment at a lower temperature of 300°C followed by slow cooling. This increase in LAGB was induced due to the fast cooling quenching process that follows the 530°C treatment instead of the slow cooling from the annealing process of the 300 °C treatment. The larger number of LAGB formed due to the increase in dislocations caused by the residual stress induced by rapid cooling.

Although the effect of different heat treatment temperatures and duration on the residual stress of AlSi10Mg had been extensively investigated, there were no reports that show a successful attempt to reduce the temperature required for a complete residual stress relief. This poses an engineering dilemma between mechanical strength and residual stress reduction, and this problem has been highlighted by several authors before (Li et al. 2016; Vaverka et al. 2018). The slow cooling process after the stress relief heat treatment significantly reduces the efficiency of the process. This study presents a novel methodology to address the problems associated with the current existing method of stress relief heat treatment. The stress relief capability of the new method and its effect on mechanical property was investigated experimentally, and verified with microstructural characterisation. This novel heat treatment methodology is capable of relieving the surface residual stress of LBPB manufactured AlSi10Mg parts without compromising its mechanical properties and at a much faster rate.

2. Novel methodology and experimental

2.1. Mechanism of residual stress reduction in novel heat treatment methodology (Bottom Heated-Uneven Air Cooling)

The novel heat treatment methodology in this experiment uses heat treatment at a lower temperature than that of the conventional method of 300°C. As the temperature used is lower than 300 °C, there will be residual stresses remaining and not completely relieved in the specimens. The specimens are then subjected to rapid and uneven cooling after the heat treatment process, thus inducing different amount of residual stress on the surfaces, either compressive or tensile. By achieving a specific uneven cooling rate at each surface of the specimen, the induced residual stresses cancel out any remaining stresses that remain after the heat treatment process, therefore achieving a complete residual stress relief on its surfaces. The physical basis of the residual stress induction mechanism proposed in this section was based on the mechanism of residual stress induction during LBPB and during rapid cooling in thermal annealing of glass.

The parabolic residual stress profile induced in tempered glass provides an insight into the mechanism of residual stress induction during rapid cooling. Upon further analysis of the parabolic residual stress curve as shown in Figure 1(a), the area bounded by the curve and x-axis in the red to green zone was found to have a ratio of 1:1. The ratio of the area of red to green zone signifies the ratio of the magnitude of the tensile force exerted in the middle region to the compressive force exerted on the top and bottom regions. This is aligned with the balance of compressive and tensile forces within a body and supports the Heyn's spring model. This also suggests that an inverse relationship exists between the residual stress magnitude and the depth of influence. As illustrated in Figure 1(b), the depth of influence in the center region in tension is larger as compared to that of the top and bottom layers in compression. As such, the tensional force in the center is spread over a larger area as compared to the compressional force acting on the relatively thinner surfaces.

During the first stage of residual stress induction in thermal tempering of glass, upon initiation of the rapid cooling process, the exposed outer surfaces contracts

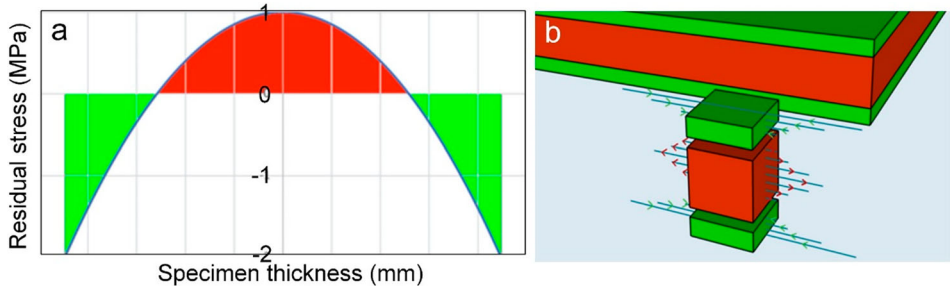

Figure 1. (a) A parabolic temperature gradient produces surface compression which is twice the interior tension in magnitude. Ratio of the area of green to red is found mathematically to be 1:1. (b) Illustration of residual stress distribution across the depth of a quenched plate. Green region denotes the region in compression and red region denotes the region in tensile stress. Rapid cooling induced on the top and bottom surfaces.

and experience restrictions due to the inner region, hence inducing tensile stress on the outer regions and compressive stress in the inner region. In the second stage, the outer surface reaches ambient temperature relatively quickly due to rapid cooling and restricts the inner contracting region, resulting in compressive stress induced on the outer surface and tensional stress in the inner region. The final magnitude of residual stress and its nature depends on the collective effect from the first and second stages. The dominance of the second stage over the first shows that the duration of time spent in each stage has a significant effect on the final magnitude and nature of residual stress induced in the part.

The illustration in Figure 2(a) shows the side view 10×4 mm face of the specimen with the 10×10 mm face placed on a heat plate. Each specimen undergoes heat treatment at temperatures 160, 200, 300, 400 and 500 °C, respectively for 2 h, immediately followed by an uneven air cooling process while still positioned on the heat plate. During the cooling process, the bottom heat plate is subjected to natural cooling from its exposed surface area to the ambient temperature as well as conduction by the specimen above it. The specimen undergoes cooling from its top surface area exposed to ambient temperature. Residual stresses will be induced due to the uneven cooling rate between the top and bottom surfaces. The heat transfer via its side surface area (10×4 mm) is assumed to be even on all 4 sides with negligible difference due to the symmetry of the shape of the specimens, hence they do not induce significant residual stress along the cross section.

The driving force of Mechanism 1 illustrated in Figure 2 (a) is the restrained contracting top region due to the bottom region. Upon the initiation of the cooling process, the top surface of the specimen is exposed to ambient air temperature while the bottom surface is in direct contact with the cooling heat plate with a higher temperature T1°C as illustrated in Figure 2(a). During the uneven cooling process, the bulk of the material at the top surface experiences induced tensile stress due to its faster rate of contraction constrained by the bottom surface. In contrast, the bottom surface experiences compressive stress due to its slower rate of contraction as illustrated in Figure 2(b). The magnitude of internal forces induced in Mechanism 1 is relatively larger than that induced in subsequent mechanisms, as the thermal gradient between the specimen itself with respect to the surrounding is at its maximum. This mechanism that takes place at the start of the cooling process is named 'Mechanism 1' as illustrated in Figure 2(b).

The driving force of Mechanism 2 illustrated in Figure 2(c) is the restrained contraction of the center layer due to the top and bottom regions. As the cooling progresses, the temperature of the upper surface of the specimen approaches that of the ambient temperature such that contraction in the upper layer becomes insignificantly small as illustrated in Figure 2(c). The region directly below the top 'non-contracting' layer continues to cool and undergoes

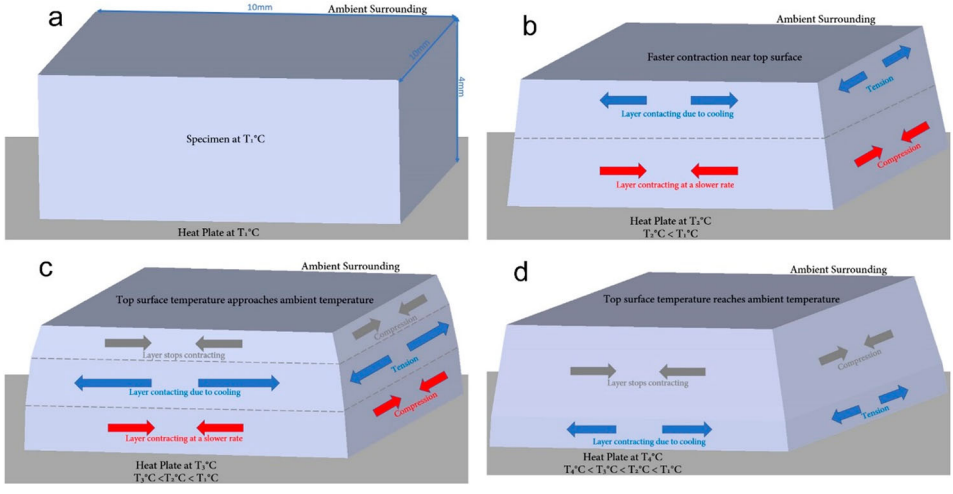

Figure 2. Mechanisms of residual stress induction from novel methodology due to uneven cooling (dimensions not to scale). The arrows denote the nature of residual stress induced in different regions of the specimen. After heat treatment (a): Illustration of the specimen on the bottom heat plate at the start of the cooling process immediately after heat treatment; Mechanism 1 (b): residual stress induction during the cooling process when the entire specimen body undergoes uneven thermal contraction; Mechanism 2 (c): Residual stress induction during the cooling process when the top surface temperature is nearing ambient temperature; and Mechanism 3 (d): Residual stress induction in the last stage when the bulk of top material is nearing ambient temperature. The length of arrow represents the relative magnitude of residual stress induced.

contraction. This contraction process is restrained by the top 'non-contracting' layer and the bottom warmer region which is contracting at a relatively slower rate due to the heat plate at the bottom. The restrain in contraction induces tensile stress on the middle region, while inducing compression stress on the top non-contracting region and the bottom slower contracting region as illustrated in Figure 2(c). The Heyn spring model (David 1999) presents the balance of internal forces within a system maintaining an equilibrium. Applying the balance of internal forces within the specimen in equilibrium, the magnitude of induced compressive force on the top and bottom region should be balanced by the tensional force in the middle contracting layer, indicating that the individual induced compressive force on the top and bottom region is relatively smaller than that of tensional force in the middle region. Given that stress is defined as the force acting on a unit area, the magnitude of the induced residual stress in each layer is dependent on the thickness of the affected region. Having induced thermal forces acting over a larger region, the induced stress is expected to be lower than if the same magnitude of thermal force were acting over a smaller region. This mechanism that takes place is named 'Mechanism 2' as illustrated in Figure 2(c).

The driving force of last stage as illustrated in Figure 2(d) is the restrained contracting layer at the bottom region due to the top region. As the cooling continues, the bulk of the top region of the specimen no longer undergo significant contraction as the thermal gradient between the material and ambient surrounding gets smaller. The lower portion of the specimen still exposed to the warm heat plate continues to cool down and continues to undergo contraction. The mismatch in contraction between the upper non-contracting region and the lower contracting portion of the material results in induced compressive stress on the top region and tensile stress on the bottom region. Similar to that of mechanism 2, applying the balance of thermal-induced force based on the Heyn spring model, the magnitude of induced tensional stress at the bottom region and compressive stress on the top region is dependent on the relative thickness of each of these two affected regions. Towards the end of the cooling process, the ratio of the non-contracting region at the top region is much larger than that of the contracting region below, suggesting that the induced compressive residual stress on the bottom surface is larger in magnitude than the compressive stress on the top surface. This mechanism that takes place towards the end of the cooling process is named 'Mechanism 3' as illustrated in Figure 2(d).

The superimposed residual stress induction from Mechanisms 1, 2 and 3 determines the magnitude and nature of the final residual stress that remains in the part. The dominance of which mechanism depends on a combination of 2 factors:

(1) The relative duration of time spent in each mechanism throughout the cooling process.
(2) The magnitude of residual stress induced in each affected region, which has an inverse relationship with the thickness of the affected layer region.

The 2 factors mentioned above are highly dependent on the treatment temperature itself and the ambient temperature. The treatment temperature determines the starting temperature of the bottom heat plate upon the initiation of the cooling process, thus affecting the thermal gradient of the heat plate with the surroundings and determining the cooling rate of the heat plate. This affects the extent of mismatch in contraction rate between the bottom region and the region above it, the thickness of the affected region, and the magnitude of induced residual stress for all three mechanisms. Higher treatment temperature will result in a longer duration spent in Mechanism 1, as it takes a longer time for the top surface of the specimen to reach near the ambient temperature for Mechanism 2. High heat treatment temperature also results in a significantly higher heat transfer rate on the top surface of the specimen, causing a larger thermal gradient to develop between the top surface and the bottom plate, therefore increasing the effects of Mechanism 3. Similarly, a lower treatment temperature will result in a longer duration spent in Mechanism 2, as a relatively shorter time is required for the top surface to reach near the ambient temperature. Lower treatment temperature also results in a lower effect from Mechanism 3 as the driving force behind this mechanism due to contraction of the bottom portion will be too small.

By optimising the heat treatment temperature, it is possible to achieve a set of induced residual stress that is capable of cancelling out the remaining residual stress in the specimens after heat treatment at a lower temperature than the vendor's suggested temperature of 300°C. In this paper, this new method will be termed the 'bottom heated-uneven air cooling' process, 'BH-UAC' in short.

2.2. Fabrication of AlSi10Mg specimens

Figure 3(a) shows the specimens used for residual stress analysis and microstructural characterisation. To simplify the effect of uneven cooling on the specimen to just the top and bottom surface, the specimens used have a relatively thin thickness with respect to their top and bottom

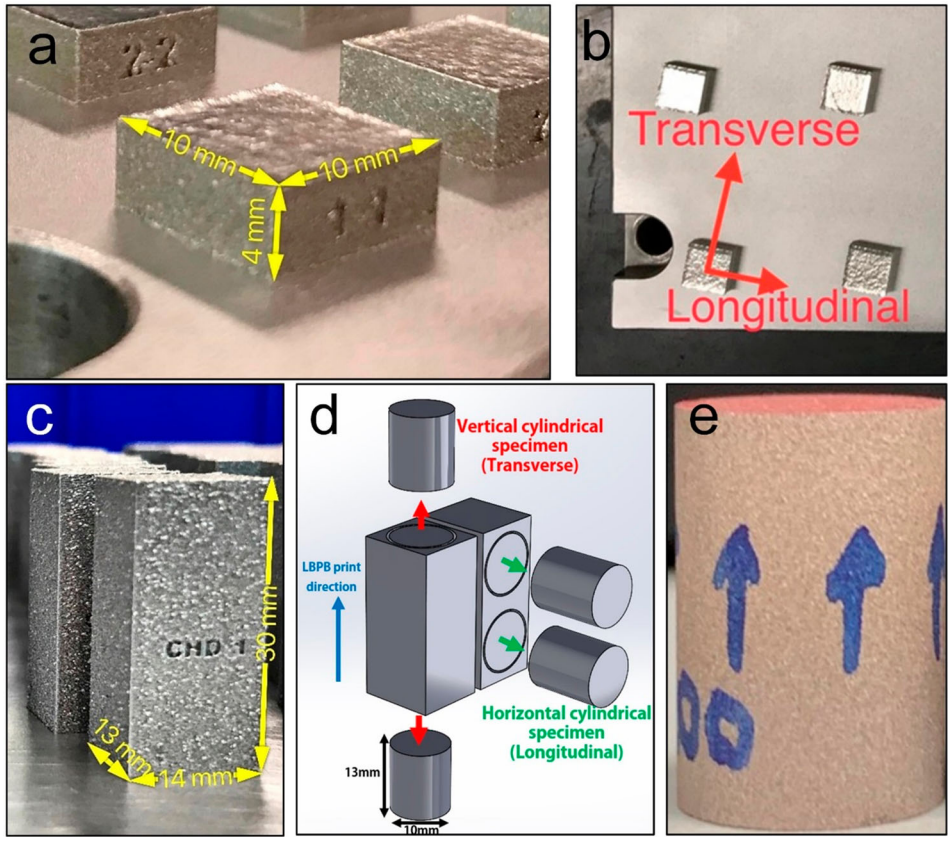

Figure 3. (a) Dimensions of specimens fabricated for residual stress and microstructural characterisation; (b) convention of the Longitudinal and Transverse direction on SLM build plate; (c) dimensions of cuboid specimens manufactured from SLM process for compressive test; (d) illustration of cylindrical specimens machined via EDM from parent specimens, in vertical and horizonal direction with respect to additive manufacturing build direction; (e) cylindrical specimen used for compression test.

surface dimensions. Figure 3(e) shows the specimens used for the compression test. Cuboid specimens were manufactured from the LBPB fusion process and cylindrical specimens were wire cut by the electrical discharge machining (EDM) process as illustrated in Figure 3(d). Transverse and longitudinal directional cylindrical specimens were used for the investigation of anisotropy after treatment at different treatment temperatures. All specimens were removed from the build plate via EDM without prior heat treatment and visible dimensional distortion.

EOS metal powder was used for the fabrication of AlSi10Mg specimens. To ensure the quality of the powder, the powder was dehumidified at 80°C for 4 h under vacuum conditions in a dehumidifying oven. The powder was sieved through a sieve mesh to remove powder particles larger than 90 µm size.

The LBPB process was performed using EOS M290, with its infill parameters based on EOS default settings for EOS AlSi10Mg powder as shown in Table 1. The alternating scan angle randomises any directional property caused by the unidirectional scan in each layer. This eliminates anisotropy of the manufactured part along with the directions perpendicular to the build direction. The combination settings used for laser power, scan speed, layer thickness, and hatch spacing equate to 73J/mm^3 of energy density used.

2.3. Residual stress characterisation – X-Ray diffraction

The X-Ray diffraction methodology was used to measure the surface residual stress of the specimens. To ensure the accuracy of the effect of treatment methodology

Table 1. Processing parameters for LBPB fusion process of AlSi10Mg samples – infill region.

Scan strategy	Stripe
Single exposure laser power (W)	370
Scan speed (mm/s)	1300
Layer thickness (µm)	30
Hatch spacing (mm)	0.13
Layer orientation angle (°)	67
Stripe width (mm)	7
Overlap stripes (mm)	0.02
Oxygen level (%)	<0.1
Re-coater speed (mm/s)	150
Preheat temperature (°C)	35

on the residual stress relief, the measurement was performed on the same specimens before and after treatment for a direct comparison. 4 readings were obtained from each specimen, namely the top and bottom surface for both longitudinal and transverse directions as illustrated in Figure 5(b). The equipment used is Xstress 3000 G3 X-ray machine by StressTech in compliance with BS EN15305:2008 non-destructive testing standard. X-ray generation was via Cr Kα radiation at 30kV and 9.0 mA at 15 s exposure, deployed on the 311 planes. Measurement was done in 13 oscillations using the $Sin^2\psi$ method the ψ angle was varied between the tilt angles −38° and +38°. The software used in the data analysis is Xtronic 1.12.0 by StressTech. The 2θ peak shift was determined using the cross-correlation method. The error bars were based on ISO/IEC Guide 98-3:2008 where the quality of the signals determines the uncertainty related to each measurement.

2.4. Comparison of novel heat treatment method with conventional annealing

The conventional annealing methodology proposed by EOS for AlSi10Mg specimens manufactured via the LBPB process is to perform heat treatment at 300 °C for 2 h for residual stress relief, followed by slow and even cooling. This process is termed 'furnace heated-slow cooling', 'FH-SC' in short. A comparison of the resulting residual stress of the novel BH-UAC method and conventional FH-SC was investigated at different treatment temperatures. The difference in variables between these two processes are – furnace heated versus bottom heated plate, and also slow cooling versus uneven air cooling.

To investigate if there is any effect of heat treatment via furnace heated versus bottom heated treatment on residual stress, a comparison of the resulting residual stress of the novel BH-UAC and FH-UAC (furnace heated-uneven air cooling) was investigated at a different treatment temperature. Specimens subjected to FH-UAC are exposed to air cooling while still positioned within the furnace itself, rested on ceramic insulation material with relatively low thermal conductivity and high heat capacity. The high heat capacity characteristics of an insulation material serve as a heat source to the specimen positioned on it, cooling down at a relatively slow rate during the cooling process, serving a similar role as that of the heat plate used in the BH-UAC process. The comparison of residual stress results between these two processes can then be used to verify if the difference in residual stress profile obtained from the novel method of BH-UAC and conventional FH-SC is due to the difference in cooling rate itself, or if the difference in heating mode (furnace versus bottom heat plate) contributed to the difference too.

Heat treatment via bottom heat plate was performed using XRD Bruker D8 Discover for the novel method of BH-UAC. The heat treatment temperature sets the surface plate temperature for the treatment itself. The treatment is performed for 2 h at temperatures of 160° C, 200°C, 300°C, 400°C and 500°C for the specimens in Figure 3(a) for comparison of the novel BH-UAC with the FH-SC and FH-UAC process. Cylindrical specimens as shown in Figure 3(e) for compressive stress test are also heat-treated at 200, 250, 275, 288, 294, 300, 400 and 500 °C with this the same setup. The cooling process takes place immediately upon the completion of the heat treatment via natural air cooling. Only one specimen undergoes heat treatment every time to ensure consistency in heat transfer. (Figure 4)

Furnace BRF 14/5-2416 by Elite Thermal Systems Limited was used for the furnace heat treatment of AlSi10Mg specimens, namely the conventional FH-SC and FH-UAC. Two different heat furnace heat treatment processes were done as follows:

- Conventional FH-SC treatment involves subjecting different specimens to 160, 200, 300 and 400 °C for 2 h, followed by controlled furnace cooling at 2°C/min.
- FH-UAC involves subjecting different specimens to 160, 200, 300, 400 and 500 °C for 2 h, after which the furnace door was opened for rapid air cooling.

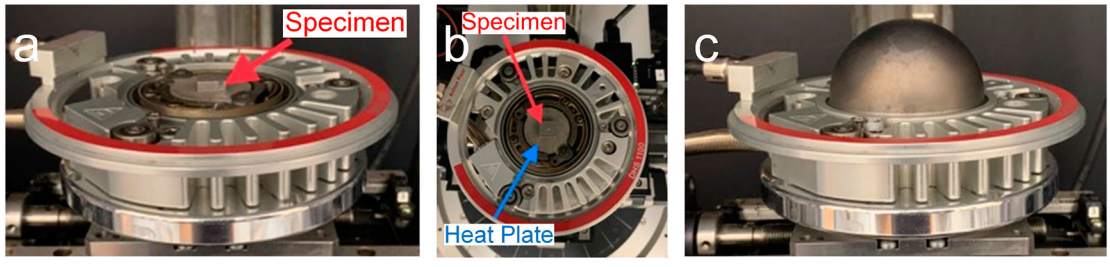

Figure 4. Setup of XRD Bruker D8 Discover for heat treatment with bottom heat plate: side view (a) and top view (b) of specimen placed on the heat plate, and graphite dome (c) to ensure even heat distribution during heat treatment.

The specimens were positioned on insulation ceramics during the heating process as well as throughout the cooling process. During cooling, the bottom ceramic act as a hot bottom surface to provide an uneven cooling condition between the top surface and the bottom surface of the specimen.

2.5. Compression test – investigation of mechanical property and anisotropy

In this experiment, the resistance to compressive loading is used as an indication of the mechanical property of the specimens in response to the novel heat treatment method at different temperatures. The effect on compressive strength of the specimens after heat treatment temperature between 250 and 300 °C was investigated to study the transition of the yield strength.

Instron 5569 electromechanical test machine was used to perform compressive tests at room temperature on the cylindrical specimens subjected to different treatment temperatures. The procedure and equipment used are in compliance with ASTM standard E9-19 (ASTM 2019). Short specimens with a length-to-diameter ratio of 1.3 according to the standard, satisfies the requirement for obtaining compressive yield strength from the experiment. The compressive force is applied up to 45kN and stopped before failure occurs, with strain values sufficient to obtain yield strength. Yield stress values are obtained from the 0.2% offset method.

2.6. Microstructural characterisation for residual stress and mechanical property changes

Cross-section polisher SM-09010 by JOEL was used to polish the AlSi10Mg samples for microstructural characterisation. The process involves milling via argon-ion accelerated at 6kV and an average beam current of 0.16mA in a vacuum environment. Keller's reagent was used to etch the polished surface for 10 s for optical microscopy and SEM.

Each specimen subjected to different heat treatment temperatures is characterised via SEM and EBSD (electron backscatter diffraction) for examining the relationship between residual stress and mechanical property changes to microstructural changes. Characterisation of samples via EBSD was performed on the top surface of the specimens. The analysis of microstructure in this study focuses on the top surface of the specimens due to the nature of the mechanism of residual stress induced as shown in Figure 2.

Material characterisation was performed using JOEL 7800F FESEM and EBSD using a backscattered electron detector by Oxford Instruments. Data acquisition and analysis were performed using the software Aztec and AztecCrystal. The top surface of the specimens which is furthest away from the bottom heated surface is selected for microstructural analysis.

3. Discussion of residual stress and mechanical property results

3.1. Comparison of residual stress reduction after novel heat treatment method versus conventional annealing at different temperature

The results from this experiment provide a direct comparison of the effect of the new novel method (BH-UAC) and the conventional method proposed by EOS (FH-SC) on the final residual stress of AlSi10Mg. The two variables used in this experiment are namely the nature of heat source – furnace environment versus heat source from a bottom plate, and the speed of cooling – slow and controlled cooling versus uneven air cooling. The effect of the nature of the heat source, however, plays an insignificant role in the nature of the residual stress induced in the results presented in Figure 5, which will be proven in the next section below. shows the resulting residual stress after 2 h of heat treatment via the conventional method of FH-SC, the new method of BH-UAC, and the average as-built residual stress without treatment after EDM cutting from the LBPB build plate. The residual stress of the as-built specimen is obtained by taking the average of the specimens used before FH-SC and BH-UAC. In as-built condition, the top surface of the specimen is compressive (−35MPa to −42MPa) in the longitudinal direction and slightly tensile (14MPa to 18MPa) in the transverse direction. The residual stress is much higher on the bottom surface (100MPa to 128MPa) in both directions. The maximum residual stress value of 128MPa is less than 50% that of the average yield strength of the material obtained from past work (Aboulkhair et al. 2016) and our result in the later section, hence there is insignificant plastic deformation due to the residual stresses.

As observed in Figure 5, the vendor EOS suggested heat treatment of 300°C via the traditional method of slow furnace cooling as the minimum temperature required for a complete residual stress relief. The resulting residual stress from heat treatment via the new BH-UAC method is represented by the orange triangular marked curve in Figure 5. As opposed to the results from the FH-SC method, the BH-UAC method achieved a residual stress relief to within ±10MPa at a lower temperature of 200 °C instead of 300 °C on the top surface

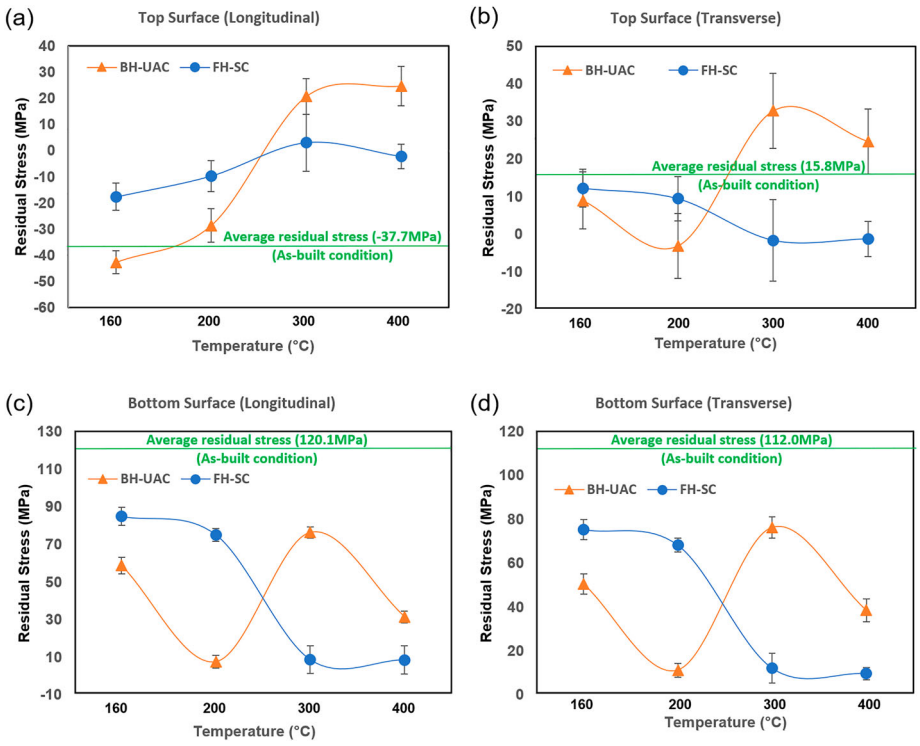

Figure 5. Effect of different heat treatment temperatures on residual stress: the novel method of BH-UAC vs convention FH-SC with respect to the original residual stress before heat treatment. (a): Top surface longitudinal direction, (b): Top surface transverse direction, (c): Bottom surface longitudinal direction, (d): Bottom surface transverse direction.

transverse, bottom surface longitudinal and transverse directions, while still having a mild stress value of −28MPa from its original average stress of −42MPa. Treatment at 300°C via the new method of BH-UAC however, induced larger tensile residual stress on all 4 readings as compared to that of 200 °C due to the effect of rapid cooling.

The new method of BH-UAC induced slight compressive stress on the top surface of the as-built specimens at a lower heat treatment temperature of 160°C while inducing tensile stress at a higher temperature of 300 and 400 °C. 200 °C appears to be the transition temperature where mild tensional and compression stress is induced on the top surface in the longitudinal and transverse direction respectively. On the bottom surface, the heat treatment process induced compressive stress for all treatment temperatures for both methods. At a low heat treatment temperature of 160 °C, Mechanism 2 is dominant in the BH-UAC method based on the mechanism discussed above, illustrated in Figure 2(c). The specimen takes a relatively shorter time for the top surface to cool down to near ambient temperature due to its low initial temperature of 160 °C. At a low treatment temperature of 160 °C, the influence of Mechanism 3 is the weakest as the driving force is lower due to the low thermal gradient between the low-temperature bottom surface and the surrounding. Hence, compressive stress was induced on the top and bottom surface at 160 °C. The compressive stress at the bottom surface is relatively larger than the top due to the combined effect of Mechanisms 1 and 2, while the compressive effect on the top surface due to Mechanism 2 is reduced due to the tensile effect from Mechanism 1.

At a higher temperature of 300 and 400 °C, the tensile effect on the top surface increases significantly as Mechanism 1 is the dominating process. The stress-induced on the bottom surface is still compressive due to the combined effect of mechanisms 1 and 2. Although the influence of Mechanism 3 increases at a higher temperature, the compressive force induced in the non-contracting region as shown in Figure 2(d) – Mechanism 3, is spread over a relatively larger area than the bottom thinner region, hence reducing the compressive stress induced on the top region. Thus, tensile residual stress is induced in the top surface at a higher temperature than at lower temperatures due to the dominating Mechanism 1. Compressive stress is still induced on the bottom surface at higher treatment temperatures but smaller in magnitude as compared to that at a lower temperature of 200°C due to the tensile effect from Mechanism 3.

3.2. Comparison of residual stress after novel heat treatment method versus furnace heated-uneven air cooling at different temperature

The experiment in this section is to validate the effect on the residual stress relief due to the nature of the heat source – heat treatment via furnace environment in FH-UAC versus heat treatment from the bottom surface of the specimen in the novel BH-UAC method. This is to verify if the results shown in Figure 5 were influenced by the speed of cooling itself or also by the nature of the heat source during the treatment. The residual stress results are presented in Figure 6.

The variance in the magnitude of the final residual stresses between the two treatment processes is attributed to the following: variance in the duration of the cooling process, the ambient as well as the bottom surface temperature. This results in a different temperature gradient, thus affecting the magnitude of residual stress-induced. The ambient temperature in the furnace is higher than that of the bottom heat plate setup during the cooling process due to the nature of the equipment and setup. The heating source of the furnace is located above the specimen which will continue to transmit heat into the ambient environment during the cooling process. In contrast, the heat source of the bottom heat treatment process is located at the bottom of the specimen on the heat plate, therefore having relatively less effect on the ambient temperature but more on the bottom surface of the specimen itself. Comparing the relative size of the heating rod in the furnace and that of the bottom heat plate, the time required for cooling is relatively longer for the furnace as compared to that of the bottom heated plate.

Similar shapes of the residual stress profile can be observed for the FH-UAC process and BH-UAC which suggests that specimens in both sets of experiments had undergone the same mechanism of residual stress induction as illustrated in Figure 2. The results in this section proved that the residual stress results observed in Figure 5 were due to the cooling speed itself and not due to the mode of heat treatment. With the results from Figure 5 and Figure 6, we can conclude the effect of uneven cooling on the trend of residual stress induced at different temperatures. Both the bottom heat plate and furnace can be used interchangeably to achieve the same mechanism of residual stress relief.

3.3. Effect of novel heat treatment method on mechanical properties

The results in this section shows the effect of the novel BH-UAC method on the compressive mechanical strength.

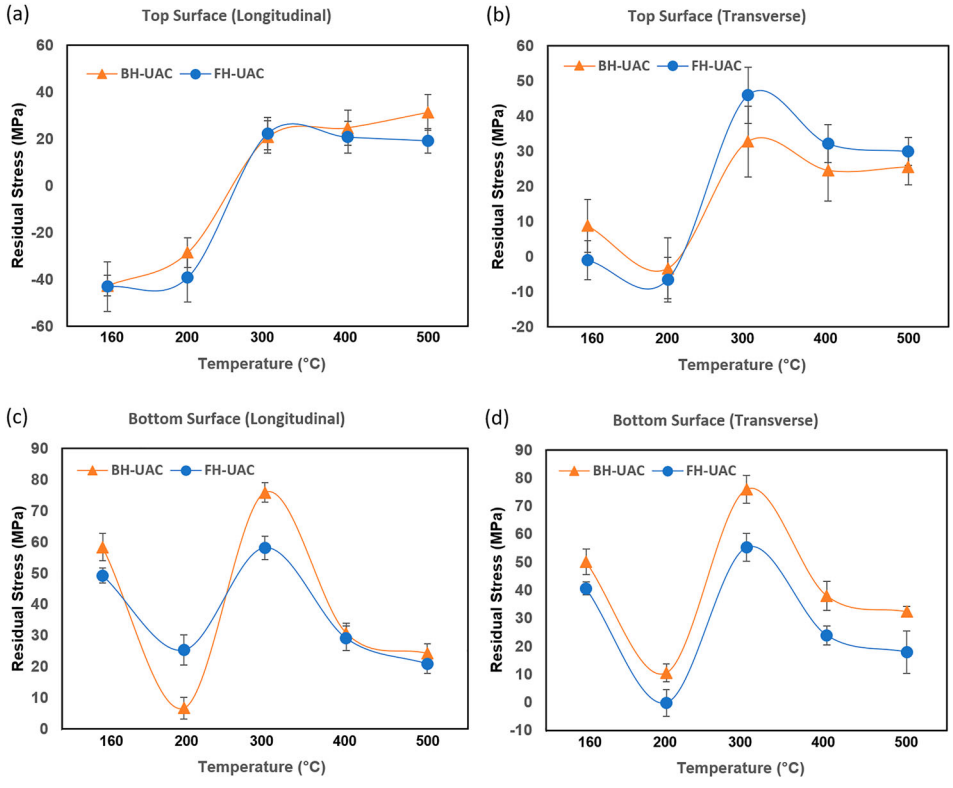

Figure 6. Effect of different heat treatment temperatures on residual stress: a novel method of BH-UAC vs FH-UAC heat treatment. (a): Top surface longitudinal direction, (b): Top surface transverse direction, (c): Bottom surface longitudinal direction, (d): Bottom surface transverse direction.

3.3.1. Compressive stress–strain curve after different treatment temperature

The effect of the treatment temperature of BH-UAC on the compressive strength of the specimens is shown in Figure 7 for longitudinal and transverse directions. As seen in Figure 7, the compressive stress–strain curves of the AlSi10Mg specimens are similar for as-built and treatment temperatures between 200 and 294 °C for both longitudinal and transverse directions, with respect to the LBPB build direction. Upon transition from 294°C to 300 °C heat treatment, the compressive strength of the specimen undergoes a drastic and sudden change with a sudden reduction in elastic modulus, and an increase in ductility. The stress–strain curves of the specimens subjected to 300, 400, and 500 °C follow a similar trend.

From the enlarged view of L1 in Figure 7(b) and T1 in Figure 7(e), the compressive stress curve for as-built and 200 °C treated temperature are identical with negligible difference. With an increase in heat treatment temperature to 250, 275, and 288 °C, there is a gradual systematic shift in the stress–strain curve upwards by approximately 10 to 15 MPa for each increment, suggesting a gradual and slight increase in compressive strength. Upon heat treatment at 294 °C, there is a slight drop in the stress–strain curve from that of 288 °C. From the enlarged view of L1 in Figure 7(b), the stress–strain curve of 294 °C starts to deviate from the common trend of the other curves from 0.075 strain onwards, portraying a slight increase in ductility.

3.3.2. Yield strength and anisotropy after different treatment temperature

The compressive yield stress also shows a sudden reduction when the heat treatment temperature changes from 294 to 300 °C as shown in Figure 8. The yield stress of the as-built specimen in the transverse direction is 308MPa, similar to the value of 317MPa obtained by Aboulkhair (Aboulkhair et al. 2016). The yield stress of as-built condition and that of 200 °C are identical in both longitudinal and transverse

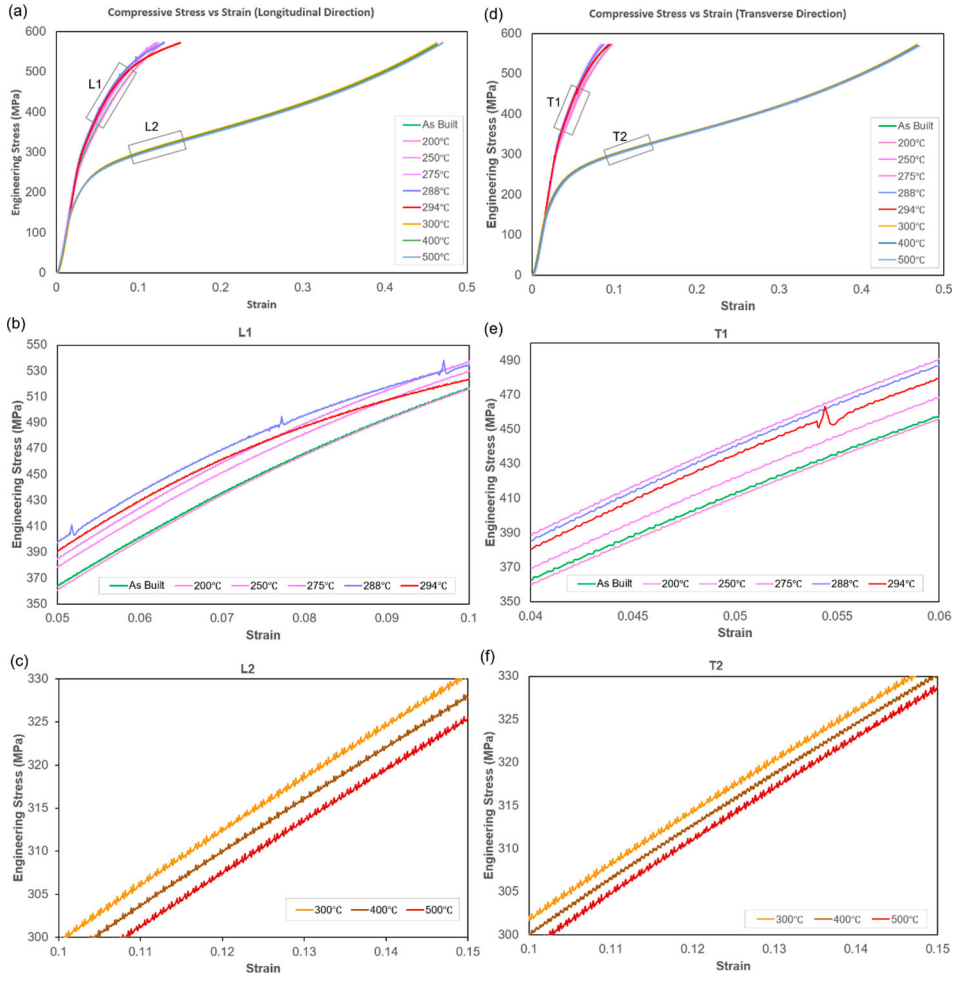

Figure 7. Compressive stress vs strain curve of AlSi10Mg specimens subjected to different heat treatment temperatures via the BH-UAC process. (a): Longitudinal direction, (b): Enlarged view of section L1, (c): Enlarged view of section L2, (d): Transverse direction, (e): Enlarged view of section T1, (f): Enlarged view of section T2.

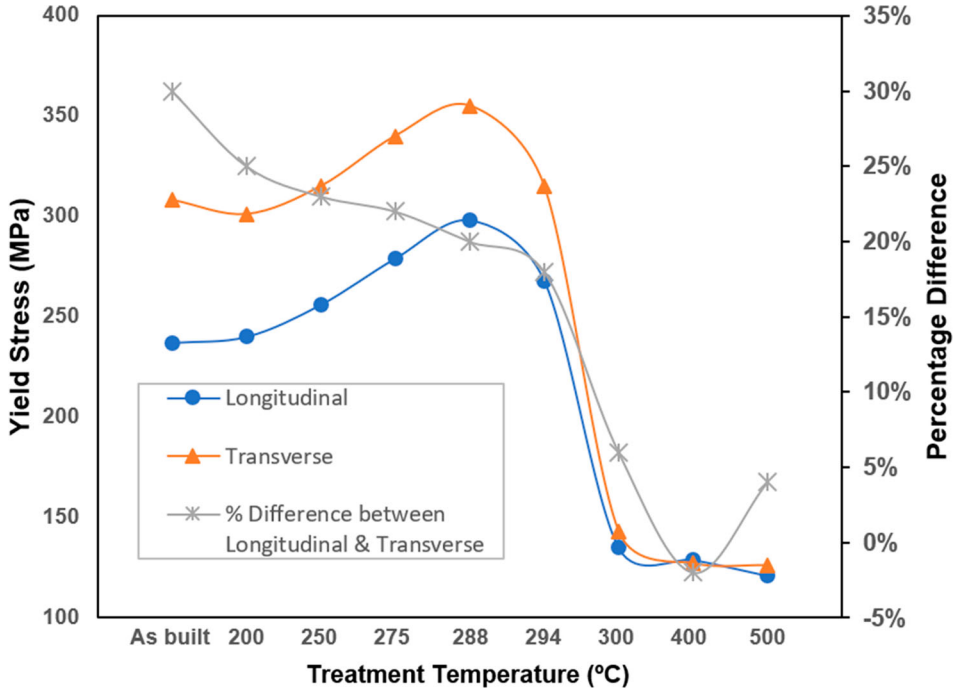

Figure 8. Effect of treatment temperature on yield stress & anisotropy.

directions differing by just 1–2%. As the treatment temperature increases from 200 to 250 °C, 275 and 288 °C, the yield strength increases as well to its maximum value at 288°C.

However, at 294°C, the specimen exhibits a slight reduction in yield stress by 10–11% in the longitudinal and transverse direction as compared to the specimen treated at 288°C. The region between 294 and 300 °C marks a transition point, where an increase of 6°C from 294 to 300 °C results in a significant reduction of yield stress by approximately 50% and 55% in the longitudinal and transverse directions respectively. The transition from 300 to 400 °C saw a slight reduction in yield stress by 6% and 11% in the longitudinal and transverse directions. From 400 to 500 °C, the yield stress changed insignificantly by 6% and 0.7% in the longitudinal and transverse directions. Comparing the yield stress reduction after treatment at 500°C with the as-built condition, the transverse yield stress was reduced by 59%, while the compressive yield stress dropped by 47% after T6 heat treatment at 520°C (Aboulkhair et al. 2016). This is attributed to the precipitation strengthening effect due to the aging process in the T6 treatment.

It was observed that anisotropy in yield strength reduced with increasing heat treatment temperature, with an abrupt reduction between 294 and 300 °C. The yield stress in the transverse direction differs from that of the longitudinal direction by approximately 30% under as-built conditions, by 25% after 200 °C treatment, and reduces gradually until 18% after treatment at 294 °C. After the transition temperature of 294 °C, the yield stress in the transverse direction differs from that of the longitudinal direction by approximately 6% after 300°C treatment, 2% after 400 °C treatment, and 4% after 500 °C treatment.

3.3.3. Remarks on compressive test results

The yield stress results suggest that heat treatment at 300 °C and above is undesirable to the compressive property of AlSi10Mg if strength is an important consideration for its functional applications. Heat treatment at 200 °C preserves the original compressive properties of the as-built condition. Treatment at 288 °C yields the largest yield strength of the material. Although anisotropy still exists relatively significantly in the parts after low-temperature heat treatment (294 °C and below), the larger yield stress after low-temperature heat treatment as compared to high-temperature treatment compensates for it.

4. Correlation of mechanical properties and residual stress with microstructure

This section presents the microstructural characterisation of the AlSi10Mg specimens at different heat treatment temperatures conducted with the BH-UAC process.

Optical Microscopy reviews the macro view of the cross-section and the top surface of the AlSi10Mg specimens shown in Figure 9. The top surface microscope image shows the scan tracks with hatch spacing of approximately 100 µm, with a layer orientation angle of

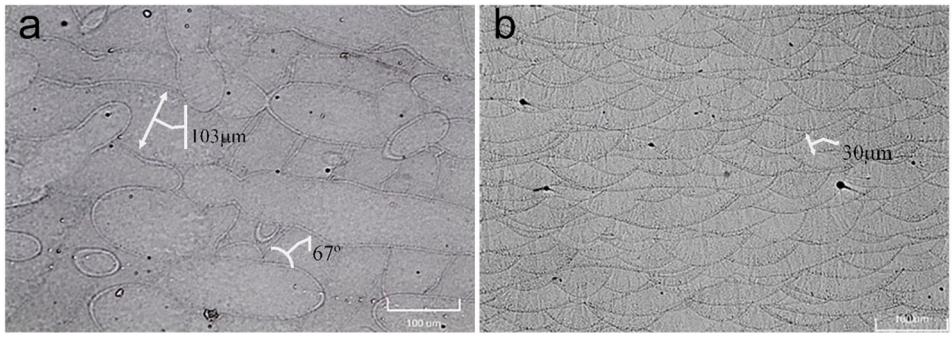

Figure 9. Optical microscope images of AlSi10Mg specimens in as-built conditions: top surface (a) and cross-sectional (b) views.

67° with respect to previous layers. The cross-sectional image shows the melt pool layer thickness to be approximately 30µm. These observations are aligned with the parameters used for the LBPB process as shown in Table 1.

4.1. Effect of si microstructure on mechanical property

The SEM images obtained for the as-built condition, 200, 294, 300, 400 and 500 °C are shown in Figure 10. The images are in the center of the scan track region where the density of the Si phase is the highest.

In line with literature reviews, AlSi10Mg specimens as built from the LBPB process are made up of cellular and nano-scale fibrous interconnected network of Si as shown in Figure 10(a). The light grey phase shows the Si eutectic phase and the darker phase shows the supersaturated α-Al matrix. Upon heat treatment to 200 °C for 2 h, the network structure of the Si phase is intact and lumps of Si structures start to form as shown in Figure 10b. While some parts of the Si network structure become thinner, some portion starts to thicken and coarsens. Figure 11 shows a high magnification view of the structure of the specimen after treatment at 288 °C, showing an increase in precipitates in between the cellular fibrous network structure which were not observed in specimens subjected to treatment at 200 °C. This increase in precipitates in between the fibrous structure contributes to the increase in yield strength of the specimens as shown in Figure 8.

Upon heat treatment to 294 °C, coarsening continues on localised parts of the Si network structure, and new formation of precipitates starts to form randomly along with the network structure as shown in the bright spots seen in Figure 10(c). The fibrous network structure at 294 °C, however, is still visible and interconnected, contributing to the mechanical strength of the material. Upon transition of heat treatment temperature from 294 to 300 °C, there is a sharp change in the Si fibrous network structure where the interconnectivity gets broken up. While the tracks of fibrous structure could still be traced, the long chains are no longer continuous.

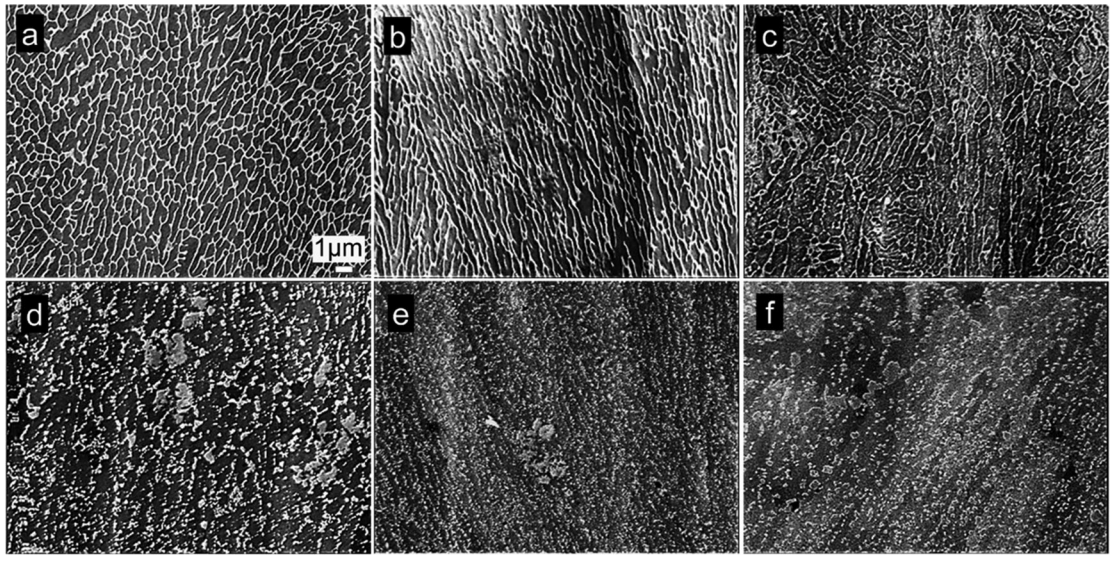

Figure 10. Secondary electron images of AlSi10Mg samples subjected to different heat treatment temperature. (a) as built condition, (b) 200°C, (c) 294°C, (d) 300°C, (e) 400°C, (f) 500°C.

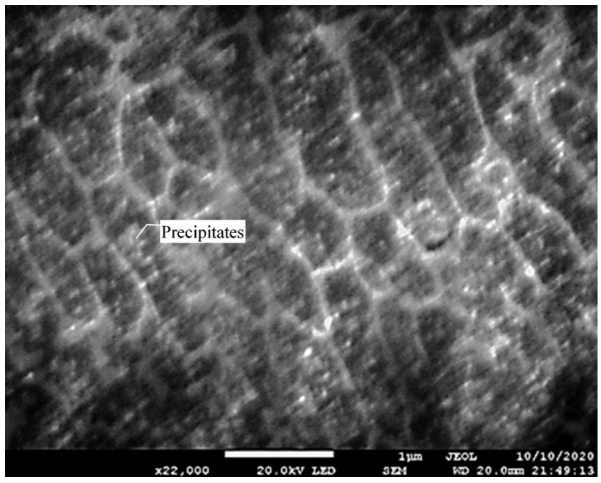

Figure 11. Secondary electron image of AlSi10Mg subjected to 288° C, showing formation of precipitates between cellular network structure of Si.

The lighter shades of grey shown in Figure 10(d) is made up of a combination of broken Si spheroid shape remaining from the previous fibrous structure and newly formed ones. At a higher heat treatment temperature of 400°C, the Si phase becomes more refined and smaller in size as seen in Figure 10(e). After 500 °C of heat treatment, the silicon particles coarsened in size as compared to that of 400 °C.

4.2. Observations of grain orientation map from EBSD

The EBSD technique was used to analyse the microstructural changes that arise due to different temperatures used for residual stress relief. The crystallographic orientation of the AlSi10Mg specimens subjected to BH-UAC treatment at different temperatures is represented by the inverse pole figures (IPF) in Figure 12.

The step size used for the EBSD scans in Figure 12 was 0.35 µm which limits the minimum grain size detectable to 0.35 µm. LAGB are defined to be between 2° and 10° denoted by the grey boundary division lines. The colours of each grain follow the inverse pole figure shown in Figure 12(a), with red, green and blue representing grains oriented towards <001>, <101> and <111> directions. While the cross-section of the specimen is made up of elongated grains from the literature review, the grains from the top surface show the projection of the cross-section of the elongated cells which are equiaxed. The melt tracks can be observed with smaller grains concentrated along-track boundaries, larger grains form up the center of scan tracks similar to past works (Liu et al. 2019). The overlay orientation angle of 67° can be observed between each melt track similar to Figure 9. Smaller grain sizes found along the intersection between each scan path were observed similar to the literature review (Yang et al. 2018; Liu et al. 2019). This is due to the repeated exposure to heat from the laser, causing repeated melting and solidification. All the specimens exhibit a preferred grain orientation in the <001> direction in the non-melt pool boundary. Grains are orientated randomly with no preferred orientation along the melt pool regions for all specimens as well. The specimens used in these experiments were manufactured with 73 J/mm^3 laser energy intensity as presented in Table 1. The grain orientation results are similar to that of

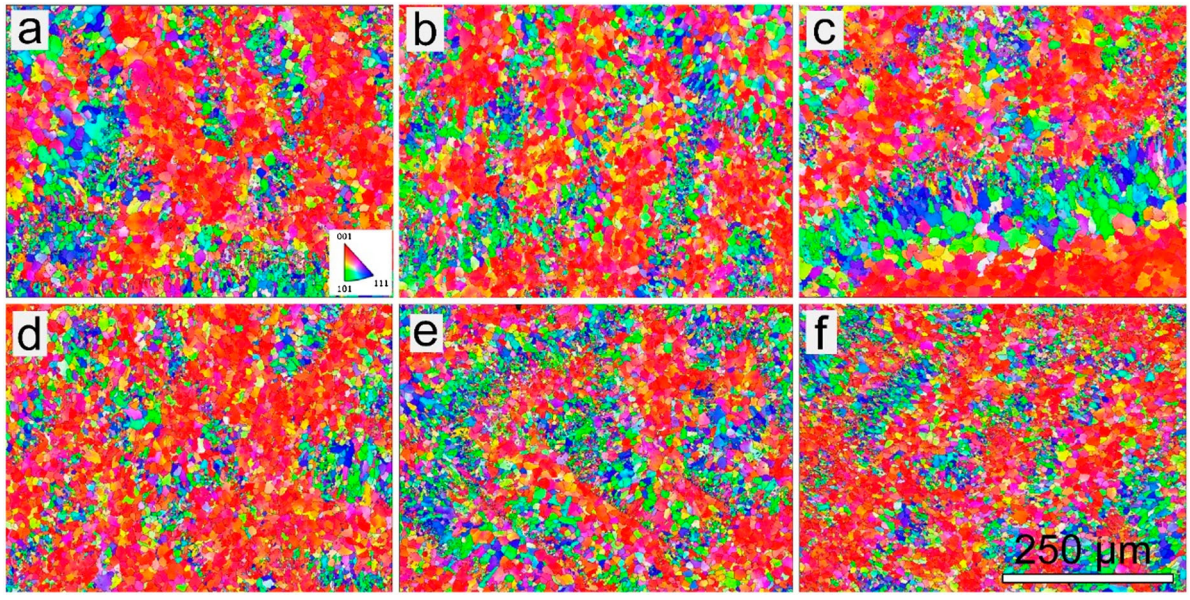

Figure 12. Inverse pole figure grain orientation and boundary map of top surface of AlSi10Mg specimen in as built condition (a), after heat treatment at 200°C (b), 294°C (c), 300°C (d), 400°C (e) and 500°C (f).

specimens manufactured with 77.8 and 100 J/mm^3 energy intensity from past works (Liu et al. 2019). Also, similar to the literature review, heat treatment has no significant effect on the grain size of AlSi10Mg (Yang et al. 2018).

4.3. Relationship between low angle grain boundaries density and grain orientation of AlSi10Mg

Figure 13 shows the semi-transparent view of the inverse pole diagram, band contrast, and boundary map of the top surface of specimens exposed to different heat treatment temperatures via BH-UAC. Low angle grains are represented via light grey colour as shown in the legend in Figure 13(a). LAGB are defined by grains with misorientation angles between 2° and 10°, while high angle grain boundaries are defined by grains with misorientation larger than 10°. The inverse pole triangle diagram showing the colour coding of each grain is also shown in Figure 13(a). It is observed that the majority of the LAGB are concentrated within grains oriented towards the build direction of <001>.

Figure 14 shows the grain orientation and boundaries map for specimens highlighting only grains orientated towards LBPB build direction of <001> within 0° to 10°, and 0° to 15° of tolerance. The inverse pole figure is shown in Figure 14(a). As seen in Figure 14(a,c,e,g,i,k), within the grains orientated in 10° variance from build direction, 52% to 61.3% of grain boundaries within these grains are LAGB, indicating a high concentration of dislocations within these grains. The density of LAGB reduces if the variance of grain orientation from <001> is increased to 15° as shown in Figure 14(b,d,f,h,j,l).

Table 2 shows the summary of the density change of LAGB in grains, and the density of grains with 10° and 15° variance from the build direction. The area of grains orientated within 10° from building direction forms up between 10.5% and 17.83% of the entire area scanned via EBSD. Increasing the variance from build direction from 10° to 15° sees a corresponding increase in the percentage of grains area between 22.68% and 35.21%, which is approximately double the area that of 10° variance. Although the amount of <001> orientated grains area doubled from 10° to 15° variance, the corresponding percentage of low angle grain within the <001> grains reduced by 21.1% to 26.9%.

The quantitative results indicate that the largest amount of low-angle grain boundaries in the specimen are concentrated in grains orientated within 10° from build direction of <001> which is aligned with the visual observation of Figure 13. The density of LAGB reduces as the orientation of the grains starts to deviate from the <001> direction. This phenomenon of having a high concentration of LAGB within the grains orientated towards LBPB build direction suggests the generation of residual stress during the grain growth stage of LBPB. Strains from the stress induced within each grain during grain growth cause dislocations within the grains.

4.4. Relationship between low angle grain boundary density and magnitude of residual stress relieve

The results in Table 2 shows that the percentage of LAGB within 10° from build direction does not reduce with an increase in heat treatment temperature. The largest density of LAGB is found in specimens subjected to treatment at 200 and 400 °C while the lowest density

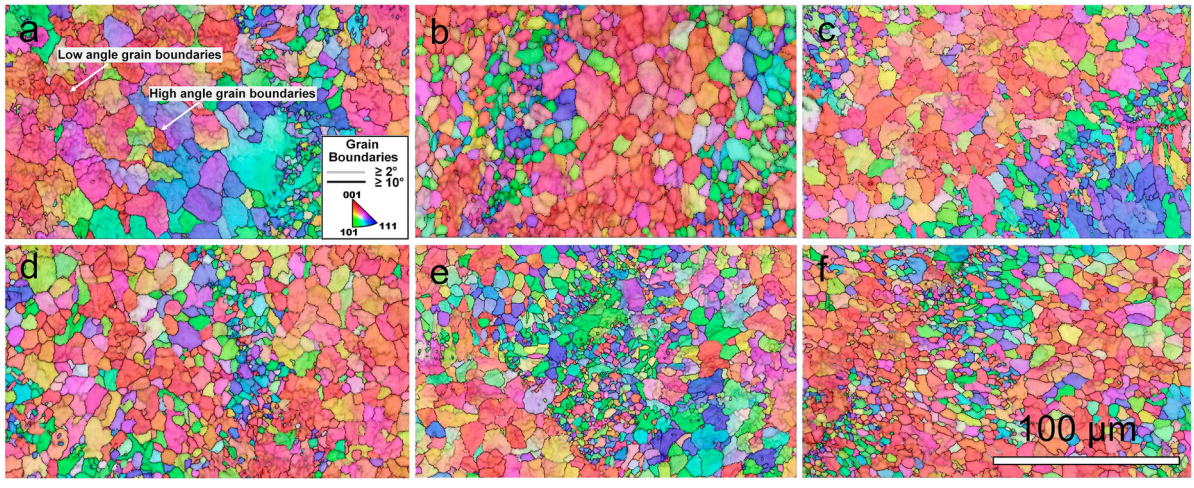

Figure 13. Semi-translucent inverse pole figure grain orientation, band contrast, and boundary map of the top surface of AlSi10Mg specimen in as built condition (a), after subjected to heat treatment at 200°C (b), 294°C (c), 300°C (d), 400°C (e) and 500°C (f).

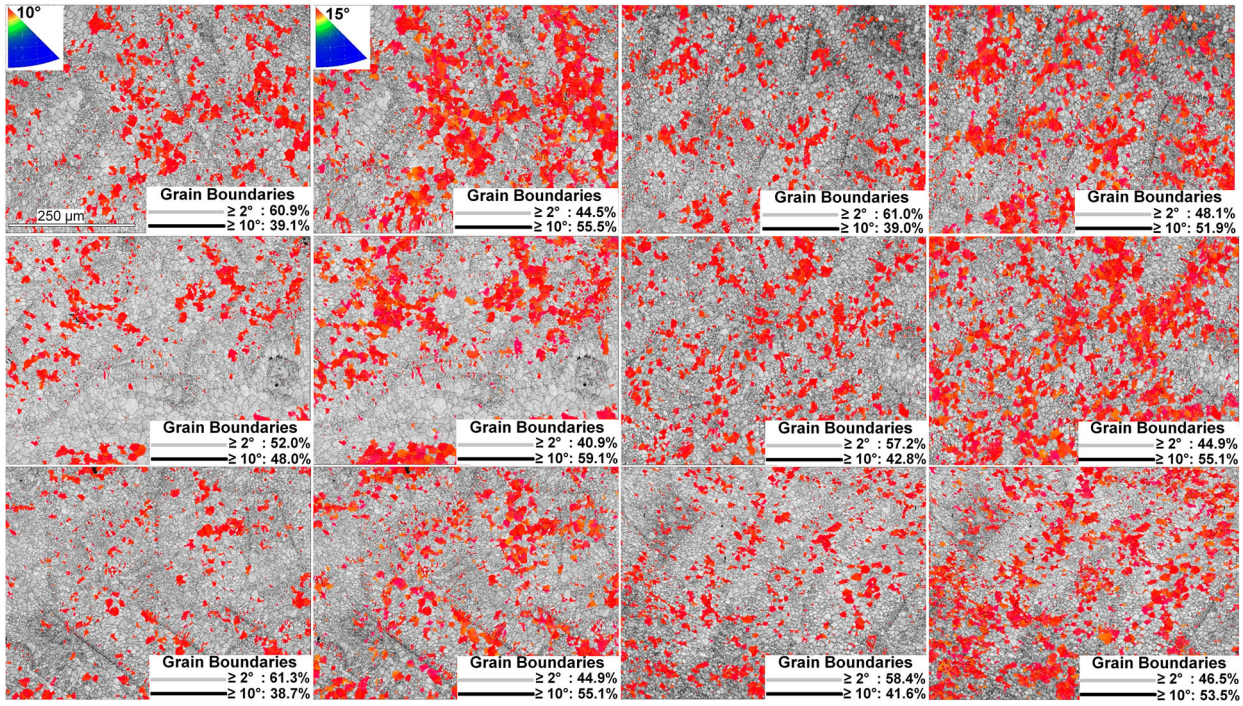

Figure 14. Grains with orientation deviation from LBPB build direction of <001> within 10°: (a), (c), (e), (g), (i), (k), and within 15°: (b), (d), (f), (h), (j), (l). Specimens in (a) and (b): as-built condition, undergone heat treatment at (c) and (d): 200°C, (e) and (f): 294°C, (g) and (h): 300°C, (i) and (j): 400°C, and (k) and (l): 500°C.

of LAGB in specimens subjected to treatment at 294 °C as shown in Figure 15.

While past works show that heat treatment will reduce the number of LAGB after heat treatment (Takata et al. 2017) due to reduction of dislocations (Humphreys and Hatherly 2012), it also shows the possible effect of induced residual stress resulting in dislocation and increase in LAGB. This is further substantiated by the results shown in Figure 15, which shows the similarity in the trend of the magnitude of stress relief induced on the specimens with the trend of percentage of low angle boundaries in <001> orientated grains. The stress relief magnitude curves of the bottom surface of the specimens shown in Figure 15 are obtained by the magnitude of the difference in residual stress of as-built condition and post-heat treatment, which represents the combined effect of the amount of thermal residual stress induced during the cooling process and stress relieved during the heat treatment. The largest effect on residual stress was after heat treatment at 200°C, which corresponds to a peak value of LAGB density. Upon heat treatment of 294 °C, the effect on residual stress dropped to a minimum, which corresponds to a minimum trough of LAGB percentage as well. A similar trend is observed with 300 and 400 °C where the effect on residual stress increases with a corresponding increase in LAGB density, with a similar drop at 500°C. This similarity in trend between LAGB density in <001> orientated grains and the residual stress effect due to heat treatment for the bottom surface, suggests that strains from the stress induction during the uneven cooling process had induced dislocations in grains orientated towards

Table 2. Percentage of LAGB in grains orientated towards build direction of LBPB, and percentage of grains with a variance of 10° and 15°.

Treatment temperature of specimen	Percentage of LAGB in grains between 0° and 10° from build direction (%)	Percentage of LAGB in grains between 0° and 15° from build direction (%)	Percentage reduction in LAGB (%)	Percentage of grains within 10° from build direction (%)	Percentage of grains within 15° from build direction (%)	Percentage increase in grains area (%)
As Built	60.9	44.5	26.9	15.36	29.63	92.9
After 200°C	61.0	48.1	21.1	14.43	27.73	92.2
After 294°C	52.0	40.9	21.3	15.81	28.3	79.0
After 300°C	57.2	44.9	21.5	17.83	35.21	97.5
After 400°C	61.3	44.9	26.8	10.5	22.68	116
After 500°C	58.4	46.5	20.4	13.85	27.85	101

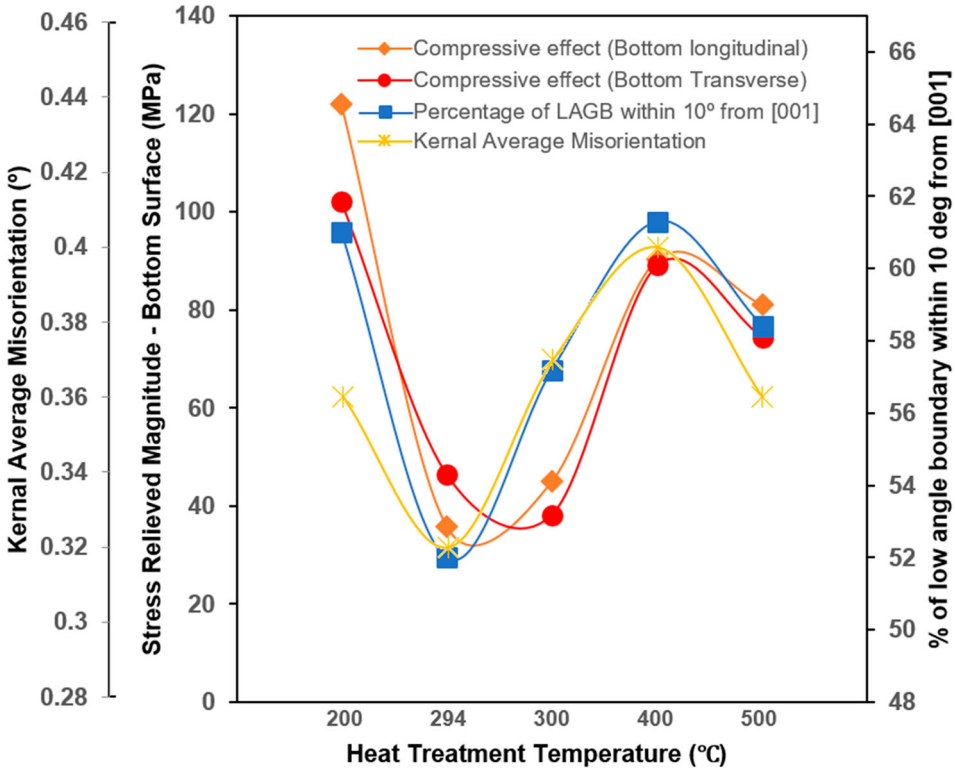

Figure 15. The similarity in the trend of KAM, percentage of LAGB within 10° from build direction, and compressive residual stress effect due to heat treatment.

<001> direction. This is further substantiated by the similar trend of the kernel average misorientation (KAM) values represented by the yellow curve in Figure 15, which suggests a corresponding increase in misorientation due to dislocations generated from induced stresses. The increase in dislocation density resulted from the concentration of stress along existing dislocations when thermal stress was induced due to rapid cooling, resulting in an increase and branching of dislocations from existing ones. A larger magnitude of residual stress induced resulted in an increase in stress concentration along dislocations, resulting in a larger density of dislocations, LAGB density and KAM. In contrast, conventional heat treatment methods for residual stress relief are based on stress relaxation and a relatively higher treatment temperature is used, allowing recovery of the material by relieving stored internal energy through dislocation motion and subsequently a corresponding reduction in dislocation density.

5. Conclusions

The novel method of BH-UAC has been proven to be capable of relieving the residual stress to ±10MPa at a lower temperature of 200 °C, as compared to the conventional annealing temperature of 300 °C and above. Although the top surface residual stress in the longitudinal direction is still at −28 MPa, this mild and compressive residual stress on the surface is much less detrimental as compared to tensile stress in terms of bending load and fatigue.

This new method not only reduces the energy required for heat treatment but also significantly reduces the duration required for the entire treatment process. The convention methodology of FH-SC requires slow and controlled cooling from 300 °C to room temperature at approximately 2 °C/min, equating to more than 2 h of cooling time. The new methodology utilises fast cooling which takes approximately 10 min to cool from 200 °C to room temperature, which is much faster than the slow cooling method.

The proposed mechanism of the residual stress induction through this novel method of heat treatment was derived based on two well established mechanisms – LBPB and the rapid cooling process in the tempering of glass. The dominance of each stage and the duration of time spent in each stage determines the final residual stress on the surface of the specimens. The nature of the resulting residual stress and magnitude obtained from experimental results are aligned with the proposed mechanism.

The compressive stress test shows that the new method of BH-UAC at 200 °C does not cause any reduction in compressive yield strength in specimens.

A sudden reduction in yield stress from 294 to 300 °C indicates an abrupt transition point between 294 and 300 °C. This is supported by the SEM images that show the destruction of the fibrous network of the Si phase taking place between 294 and 300 °C. Compressive yield strength was found to be at its peak after treatment at 288 °C, which was contributed to the increased precipitation in between the fibrous network of the Si phase. Anisotropy was found to reduce with increasing temperature, and also undergoes an abrupt reduction in the transition from 294 to 300 °C. However, anisotropy still exists in the specimen after being subjected to the new BH-UAC process at 200 °C.

LAGB was observed to concentrate in grains orientated towards the build direction of the LBPB process. A relationship was found with EBSD results showing a similar trend in LAGB concentration with the residual stress induced due to rapid cooling after treatment at different temperatures. A larger magnitude of residual stress induced using the new method of BH-UAC leads to a larger strain and subsequently causes dislocations, which corresponds to an increase in LAGB density and also a higher KAM value.

Compared with the conventional method of heat treatment of FH-SC, while this new method of BH-UAC is successful in relieving residual stress at a lower temperature, requires less cooling time, and retains the original compressive strength in as-built condition, it also comes with a compromise of anisotropy. Depending on the requirements and applications of the functional part this material is to be used for, the novel method of BH-UAC will be useful if anisotropy plays a less significant consideration where compressive loading is more significant.

Disclosure statement

No potential conflict of interest was reported by the author(s).

Funding

This research was supported by Makino Asia Pte Ltd [account no. 04IDS000476N035] through the Economic Development Board Industrial Postgraduate Programme and the National Research Foundation, Prime Minister's Office, Singapore under its Medium-Sized Centre funding scheme. This work was also supported by the Singapore Centre for 3D Printing (SC3DP), School of Mechanical and Aerospace Engineering (MAE), Nanyang Technological University (NTU), and Advanced Remanufacturing and Technological Center (ARTC) [account no. 04SBS000515C160], Agency for Science, Technology and Research (A*STAR), Singapore, through the use of its additive manufacturing facilities.

Notes on contributors

Chong Heng Lim is a research fellow in the School of Mechanical Engineering, National University of Singapore, Singapore.

Hua Li is a professor in the School of Mechanical and Aerospace Engineering, Nanyang Technological University, Singapore.

Manickavasagam Krishnan is a technical lead in the Additive Manufacturing Industrialisation Department of the Advanced Remanufacturing and Technology Centre (ARTC), Singapore.

Kewei Chen is a research associate in the School of Mechanical and Aerospace Engineering, Nanyang Technological University, Singapore.

Junru Li is a lecturer in the School of Electromechanical Engineering, Qingdao University, China.

ORCID

Chong Heng Lim http://orcid.org/0000-0003-2005-368X
Hua Li http://orcid.org/0000-0003-4899-9477
Manickavasagam Krishnan http://orcid.org/0000-0002-9631-3399
Kewei Chen http://orcid.org/0000-0003-1731-8034
Junru Li http://orcid.org/0000-0002-7478-8342

References

Aboulkhair, Nesma T., Ian Maskery, Chris Tuck, Ian Ashcroft, and Nicola M. Everitt. 2016. "The Microstructure and Mechanical Properties of Selectively Laser Melted AlSi10Mg: The Effect of a Conventional T6-Like Heat Treatment." *Materials Science and Engineering: A* 667: 139–146. doi:10.1016/j.msea.2016.04.092.

ASTM, E9. 2019. *Standard Test Methods of Compression Testing of Metallic Materials at Room Temperature*. West Conshohocken, PA: ASTM International, 98–105.

Aydıner, Cahit, and Ersan Ustundag. 2005. "Residual Stresses in Bulk Metallic Glasses due to Thermal Tempering." *Materials Science Forum - MATER SCI FORUM* 490-491: 515–520. doi:10.4028/www.scientific.net/MSF.490-491.515.

Benachour, M., N. Benachour, and M. Benguediab. 2016. "Effect of Compressive Residual Stress Generated by Plastic Preload on Fatigue Initiation of 6061 Al-Alloy." In *21st European Conference on Fracture*, edited by F. Iacoviello, L. Susmel, D. Firrao, and G. Ferro, 3090–3097. Amsterdam: Elsevier Science Bv.

David, Kirk. 1999. "Shot Peening." *Aircraft Engineering and Aerospace Technology* 71 (4): 349–361. doi:10.1108/00022669910270727.

Dong, Ya-Bo, Wen-Zhu Shao, Jian-Tang Jiang, Bao-You Zhang, and Liang Zhen. 2015. "Minimization of Residual Stress in an Al-Cu Alloy Forged Plate by Different Heat Treatments." *Journal of Materials Engineering and Performance* 24 (6): 2256–2265. doi:10.1007/s11665-015-1505-2.

Frazier, W. E. 2014. "Metal Additive Manufacturing: A Review." *Journal of Materials Engineering and Performance* 23 (6): 1917–1928. doi:10.1007/s11665-014-0958-z.

Humphreys, Frederick John, and Max Hatherly. 2012. *Recrystallization and Related Annealing Phenomena*. New York: Elsevier.

Iida, K., S. Yamamoto, and M. Takanashi. 1997. "Residual Stress Relaxation by Reversed Loading." *Welding in the World/ Le Soudage Dans le Monde* 39 (3): 138–144.

Karlsson, L. 2005. "Residual Stresses Due to Welding of a Nozzle to a Pressure Vessel." PhD diss., Division of Solid Mechanics, Lund University.

Karolus, Małgorzata, Joanna Maszybrocka, Andrzej Stwora, and Grzegorz Skrabalak. 2019. "Residual Stresses of alsi10mg Fabricated by Selective Laser Melting (SLM)." *Archives of Metallurgy and Materials* 64: 1011–1016.

Kruth, J. P., P. Mercelis, J. Van Vaerenbergh, L. Froyen, and M. Rombouts. 2005. "Binding Mechanisms in Selective Laser Sintering and Selective Laser Melting." *Rapid Prototyping Journal* 11 (1): 26–36. doi:10.1108/13552540510573365.

Kudryavtsev, P. I. 1964. "Residual Welding Stresses and Strength of Joints [in Russian]." *Mashinostroenie, Moscow*.

Li, Wei, Shuai Li, Jie Liu, Ang Zhang, Yan Zhou, Qingsong Wei, Chunze Yan, and Yusheng Shi. 2016. "Effect of Heat Treatment on AlSi10Mg Alloy Fabricated by Selective Laser Melting: Microstructure Evolution, Mechanical Properties and Fracture Mechanism." *Materials Science and Engineering: A* 663: 116–125. doi:10.1016/j.msea.2016.03.088.

Liu, Y., Y. Q. Yang, and D. Wang. 2016. "A Study on the Residual Stress During Selective Laser Melting (SLM) of Metallic Powder." *International Journal of Advanced Manufacturing Technology* 87 (1-4): 647–656. doi:10.1007/s00170-016-8466-y.

Liu, Xihe, Congcong Zhao, Xin Zhou, Zhijian Shen, and Wei Liu. 2019. "Microstructure of Selective Laser Melted AlSi10Mg Alloy." *Materials & Design* 168: 107677. doi:10.1016/j.matdes.2019.107677.

Maamoun, Ahmed H., Mohamed Elbestawi, Goulnara K. Dosbaeva, and Stephen C. Veldhuis. 2018. "Thermal Post-Processing of AlSi10Mg Parts Produced by Selective Laser Melting Using Recycled Powder." *Additive Manufacturing* 21: 234–247. doi:10.1016/j.addma.2018.03.014.

Manfredi, Diego, Flaviana Calignano, Manickavasagam Krishnan, Riccardo Canali, Elisa Ambrosio, Sara Biamino, Daniele Ugues, Matteo Pavese, and Paolo Fino. 2014. "Additive Manufacturing of Al Alloys and Aluminium Matrix Composites (AMCs)." In.

McClung, R. C. 2007. "A Literature Survey on the Stability and Significance of Residual Stresses During Fatigue." *Fatigue & Fracture of Engineering Materials & Structures* 30 (3): 173–205. doi:10.1111/j.1460-2695.2007.01102.x.

Mercelis, Peter, and Jean-Pierre Kruth. 2006. "Residual Stresses in Selective Laser Sintering and Selective Laser Melting." *Rapid Prototyping Journal* 12 (5): 254–265. doi:10.1108/13552540610707013.

Mertens, Anne, Olivier Dedry, David Reuter, Olivier Rigo, and Jacqueline Lecomte-Beckers. 2015. "Thermal Treatments of AlSi10Mg Processed by Laser Beam Melting." In: *Proceedings of the 26th International Solid Freeform Fabrication Symposium*.

Morgan, R., C. J. Sutcliffe, and W. O'Neill. 2004. "Density Analysis of Direct Metal Laser re-Melted 316L Stainless Steel Cubic Primitives." *Journal of Materials Science* 39 (4): 1195–1205. doi:10.1023/B:JMSC.0000013875.62536.fa.

Mukherjee, T., J. S. Zuback, A. De, and T. DebRoy. 2016. "Printability of Alloys for Additive Manufacturing." *Scientific Reports* 6), doi:10.1038/srep19717.

Padovano, Elisa, Claudio Badini, Anna Pantarelli, Flavia Gili, and Fabio D'Aiuto. 2020. "A Comparative Study of the Effects of Thermal Treatments on AlSi10Mg Produced by Laser Powder bed Fusion." *Journal of Alloys and Compounds* 831: 154822. doi:10.1016/j.jallcom.2020.154822.

Panontin, T. L., and M. R. Hill. 1996. "The Effect of Residual Stresses on Brittle and Ductile Fracture Initiation Predicted by Micromechanical Models." *International Journal of Fracture* 82 (4): 317–333. doi:10.1007/bf00013236.

Rafieazad, Mehran, Mohsen Mohammadi, and Ali M. Nasiri. 2019. "On Microstructure and Early Stage Corrosion Performance of Heat Treated Direct Metal Laser Sintered AlSi10Mg." *Additive Manufacturing* 28: 107–119. doi:10.1016/j.addma.2019.04.023.

Reid, L. 2003. "Sustaining an Aging Aircraft Fleet With Practical Life Enhancement Methods." In: *Proceedings at the RTO Applied Vehicle Technology Panel Specialists' Meeting*, St. Joseph Print Group Inc., eds., Ottawa, ON, Canada, October 8–11, Vol. 32, pp. 1–10, October 8–11.

Shanmughasundaram, Palanisamy, and Arne K. Dahle. 2018. *"Heat Treatment of Aluminum Alloys*." In Reference Module in Materials Science and Materials Engineering*. Amsterdam: Elsevier.

Siddique, M. 2005. "*Experimental and Finite Element Investigation of Residual Stresses and Distortions in Welded Pipe-flange Joints*." Ph.D. diss., Ghu-lam Ishaq Khan Institute of Engineering Sciences and Technology.

Takata, Naoki, Hirohisa Kodaira, Keito Sekizawa, Asuka Suzuki, and Makoto Kobashi. 2017. "Change in Microstructure of Selectively Laser Melted AlSi10Mg Alloy with Heat Treatments." *Materials Science and Engineering: A* 704: 218–228. doi:10.1016/j.msea.2017.08.029.

Varshneya, Arun K., and John C. Mauro. 2019. "Chapter 13 - Glass Transition Range Behavior." In *Fundamentals of Inorganic Glasses (Third Edition)*, edited by Arun K. Varshneya, and John C. Mauro, 293–382. Amsterdam: Elsevier.

Vaverka, O., D. Koutný, R. Vrána, L. Pantelejev, and D. Paloušek. 2018. "Effect of Heat Treatment on Mechanical Properties and Residual Stresses in Additively Manufactured Parts." In: *Proceedings of the Engineering Mechanics 2018 24th International Conference, Svratka, Czech Republic*.

Withers, P. J., and Hkdh Bhadeshia. 2001. "Overview - Residual Stress Part 1 - Measurement Techniques." *Materials Science and Technology* 17 (4): 355–365.

Yan, Qian, Bo Song, and Yusheng Shi. 2020. "Comparative Study of Performance Comparison of AlSi10Mg Alloy Prepared by Selective Laser Melting and Casting." *Journal of Materials Science & Technology* 41: 199–208. doi:10.1016/j.jmst.2019.08.049.

Yang, Kun V., Paul Rometsch, C. H. J. Davies, Aijun Huang, and Xinhua Wu. 2018. "Effect of Heat Treatment on the Microstructure and Anisotropy in Mechanical Properties of A357 Alloy Produced by Selective Laser Melting." *Materials & Design* 154: 275–290. doi:10.1016/j.matdes.2018.05.026.

Zhang, Meixia, Changmeng Liu, Xuezhi Shi, Xianping Chen, Cheng Chen, Jianhua Zuo, Jiping Lu, and Shuyuan Ma. 2016. "Residual Stress, Defects and Grain Morphology of Ti-6Al-4V Alloy Produced by Ultrasonic Impact Treatment Assisted Selective Laser Melting." *Applied Sciences* 6 (11): 304.

Zhuo, Longchao, Zeyu Wang, Hongjia Zhang, Enhuai Yin, Yanlin Wang, Tao Xu, and Chao Li. 2019. "Effect of Post-Process Heat Treatment on Microstructure and Properties of Selective Laser Melted AlSi10Mg Alloy." *Materials Letters* 234: 196–200. doi:10.1016/j.matlet.2018.09.109.